Astronomy & Astrophysics manuscript no. output
June 25, 2026

Formation of multiple dust rings and gaps in protoplanetary discs by a single migrating planet

Radiative discs and observational signatures

K. M. Weiskopf[1], S. C. Meiners[2], A. Ziampras[1,3] and C. P. Dullemond[2]

[1] Ludwig-Maximilians-Universität München, Universitäts-Sternwarte, Scheinerstr. 1, 81679 München, Germany
[2] Institute for Theoretical Astrophysics, centre for Astronomie (ZAH), Heidelberg University, Albert Ueberle Str. 2, 69120 Heidelberg,
[3] Max Planck Institute for Astronomy, Königstuhl 17, 69117 Heidelberg, Germany Germany

Received XX, 20XX

ABSTRACT

Context. Dust structures in protoplanetary discs have been widely observed, and their creation remains an active field of research. Several possible origins have already been explored, including magnetohydrodynamic processes, shadows, and planet–disc interactions.
Aims. The goal of this paper is to investigate whether a single migrating planet in a low-viscosity disc, including radiative processes, is capable of generating observable dust structures. We examine both the lifetime of such structures and potential asymmetries within them.
Methods. We performed a set of high-resolution, two-dimensional hydrodynamic simulations of migrating planets using three different equations of state: isothermal, constant β-cooling, and an adaptive β model. We included dust in all simulations and post-processed the resulting dust density profiles to create radiative transfer images.
Results. For all equations of state considered, the planet undergoes one or several migration jumps, each producing dust rings and gaps. The lifetime of these structures depends on the phase of slow migration preceding and occurring between jumps, but in all cases they remain visible for at least 400 kyr. We find that cooling has a decisive effect on the migration behaviour and the number of jumps, but no measurable influence on the lifetime of the dust structures. The structures exhibit relatively few asymmetries and large-scale vortices persist for an average of only 90 kyr.
Conclusions. Our models highlight the ability of planets to open multiple gaps while migrating and stress the importance of a realistic cooling model. Care should be taken when interpreting and comparing such models directly with observations.

Key words. accretion, accretion discs – hydrodynamics – methods:numerical – planet-disc interactions – radiation-dynamics

1. Introduction

The Disk Substructures at High Angular Resolution Project (DSHARP) survey (Andrews et al. 2018) observed the $\lambda = 1.25$ mm continuum and ^{12}CO J $= 2-1$ line emission of 20 nearby protoplanetary discs. They confirm without doubt that the brightest and largest protoplanetary discs can contain visible dust rings and gaps, as well as asymmetries in their dust profile. At $\lambda \approx 1.25$ mm, the emission is dominated by thermal radiation from millimetre-sized dust grains in the disc mid-plane, which allows identification of disc substructures. Similar observations have also been reported by the Ophiuchus DIsk Survey Employing ALMA (ODISEA) (Orcajo et al. 2025), exoALMA (Teague et al. 2025), the Molecules with ALMA at Planet-forming Scales (MAPS) (Öberg et al. 2021), and the ALMA survey of the Lupus (Ansdell et al. 2018) and Taurus (Long et al. 2018) star-forming regions. A better understanding of the formation of these dust structures would provide a deeper insight into the dynamics of the disc.

Several theoretical formation mechanisms to explain the development of substructure have been identified. These mechanisms include the formation of pressure bumps at the inner edge of the dead zone (Armitage et al. 2001; Varnière & Tagger 2006; Flock et al. 2015; Flock et al. 2017; Roberts et al. 2025), spontaneous dust ring formation due to the streaming instability (Youdin & Goodman 2005; Ostertag & Flock 2025), differential radial drift (Jiang & Ormel 2023), magnetic effects (Béthune et al. 2016; Riols et al. 2020), thermal instabilities (Ueda et al. 2021; Sudarshan et al. 2026; Owen 2020), warps (Smallwood et al. 2024a,b), and shadow-driven structures (Su & Bai 2024; Qian & Wu 2024; Ziampras et al. 2025a; Zhang et al. 2025).

Another commonly proposed explanation is the presence of embedded planets. They launch spiral waves due to a resonance between the planet's gravitational potential and the epicyclic motion of the disc material (Goldreich & Tremaine 1979; Ogilvie & Lubow 2002). For sufficiently high planetary masses or low disc viscosities, the excited spiral waves steepen into shocks, clearing material from the planet's vicinity and thus opening a gap (Goodman & Rafikov 2001; Rafikov 2002). Zhang et al. (2018); Miranda & Rafikov (2020a); Zhang & Zhu (2020), and Ziampras et al. (2020) show that a single non-migrating planet can open multiple gaps and study the effects of radiative processes on gap formation.

McNally et al. (2019) (hereafter Mc19) and later Wafflard-Fernandez & Baruteau (2020) (hereafter WB20), who considered higher viscosities, investigated the migration of a single

Article published by EDP Sciences, to be cited as https://doi.org/10.1051/0004-6361/202660413

planet in an isothermal disc and discovered migration jumps, referred to as 'intermittent migration'. These jumps can create dust ring and gap structures, which remain visible when plotting the continuum emission at (sub)millimetre wavelengths. Meiners et al. (2026) (hereafter M26) continued the analysis of migration, covering different aspect ratios and viscosities, and disabling the gas self-gravity in all simulations. They also observed intermittent migration jumps, further confirming their existence. In general, planetary migration is highly dependent on the level of turbulence within the disc, typically modelled as an effective 'viscosity' with an α parameter (Shakura & Sunyaev 1973). For $\alpha \gtrsim 10^{-3}$, planets migrate in the classical type-I and type-II regimes (Paardekooper et al. 2011; Kley & Nelson 2012), depending on whether they can open a gap. Type-I migration is driven by an interplay of Lindblad and corotation torques, resulting in rapid migration. For an Earth-sized planet, this corresponds to a migration timescale of $\tau_{mig} \sim 10^5$ yr (Kley & Nelson 2012).

If the planet opens a sufficiently deep gap and clears its corotation region, only very few Lindblad modes act, which produces a negligible net torque. Kley & Nelson (2012) suggest that the planet is now coupled with the viscous evolution of the disc, as the deep gap prevents material from entering the inner disc. On the other hand, Dürmann & Kley (2015) found that the planet only prevents gas from crossing the gap in its immediate vicinity, challenging the idea that the planet is coupled to the viscous evolution. This results in migration rates that differ significantly from the viscous timescale. Furthermore, Scardoni et al. (2022) show that a planet in the type-II regime might switch from inward to outward migration, decoupled from the viscous evolution, but still migrating with a similar rate. Additionally, a planet might undergo phases of very rapid migration, which are often labelled as type-III migration (Masset & Papaloizou 2003; Rometsch et al. 2020).

In recent years, a number of studies have suggested that the disc's viscosity takes lower values, with a median around $\alpha \sim 10^{-4}$ (Villenave et al. 2022; Dullemond et al. 2018; Rosotti 2023), but its value remains a topic of discussion. We further acknowledge that inferring viscosity values from observations comes with limitations. Ziampras et al. (2025b) (hereafter Z25) introduced new migration regimes in these nearly inviscid discs, which emerge for planets in a certain mass range. Hence, migration is more diverse than previously thought.

As a continuation of Mc19 and M26 work, the goal of this paper is to investigate the ability of a single planet to open multiple gaps while including radiative processes on the disc. We tailor our setups to model the outer disc, ensuring comparability with ALMA observations. We further analyse the lifetime and appearance of the created rings and gaps and assess the observability of these structures.

In Sect. 2 we introduce our physical model and numerical framework. We present our results in Sect. 3 and discuss them in Sect. 4. We present our conclusions in Sect. 5.

2. Physics and numerics

In this section, we briefly describe the physical model and numerical setup. We adopted our radiative cooling model from Ziampras et al. (2023) and summarise it below.

2.1. Physical model

We modelled a vertically integrated disc around a central star. The gas is assumed to be ideal with a surface density Σ, internal energy e, and velocity $\boldsymbol{u}$. Its equations of motion are given by the Navier–Stokes equations in cylindrical coordinates $\{R, \phi\}$ with the adiabatic index γ:

$$\frac{\partial \Sigma}{\partial t} + \boldsymbol{u} \cdot \nabla \Sigma = -\Sigma \nabla \cdot \boldsymbol{u}, \tag{1}$$

$$\Sigma \frac{\partial \boldsymbol{u}}{\partial t} + \Sigma(\boldsymbol{u} \cdot \nabla)\boldsymbol{u} = -\nabla P - \Sigma \boldsymbol{g} + \nabla \cdot \bar{\sigma}, \tag{2}$$

$$\frac{\partial \Sigma e}{\partial t} + \nabla \cdot (\Sigma e \boldsymbol{u}) = -P \nabla \cdot \boldsymbol{u} - \Sigma c_{\mathrm{v}} \frac{T - T_0}{\beta} \Omega_{\mathrm{K}}. \tag{3}$$

Here, $\bar{\sigma}$ denotes the viscous stress tensor and $P = (\gamma - 1)\Sigma e$ denotes the vertically integrated pressure. The isothermal sound speed is given by $c_{\mathrm{s}} = \sqrt{P/\Sigma} = \sqrt{\mathcal{R}T/\mu}$, with the mean molecular mass $\mu = 2.35$. We define a pressure scale height $H = c_{\mathrm{s}}/\Omega_{\mathrm{K}}$, with a Keplerian frequency $\Omega_{\mathrm{K}} = \sqrt{\mathrm{G}M_*/R^3}$. The aspect ratio h is given by $h = H/R$, where R is the radial distance to the central star. The viscosity follows the model from Shakura & Sunyaev (1973), with $\nu = \alpha c_{\mathrm{s}} H$. We define the vorticity $\omega = \boldsymbol{\nabla} \times \boldsymbol{u}$ and the inverse vortensity ($\mathcal{IV}$) of the gas as

$$\mathcal{IV} = \frac{\Sigma}{\omega}. \tag{4}$$

We used this quantity to confirm the existence of small vortices in the disc, which present as local maxima. We used the inverse vortensity, since it scales with the coorbital mass deficit, which is related to intermittent migration, scales with $\mathcal{IV}$ (Masset & Papaloizou 2003; Wafflard-Fernandez & Baruteau 2020).

We did not include viscous heating because the paper focuses on planets predominately in the outer regions of the disc. Following Ziampras et al. (2023) and Miranda & Rafikov (2020a), we defined cooling timescales for radiative loss from the surface (hereafter surface cooling), cooling of the mid-plane through radial radiative diffusion (now mid-plane cooling), and flux-limited diffusion (FLD). Estimating a cooling timescale using $t_{\mathrm{cool}} \sim e/\dot{e}$ (Ziampras et al. 2020) results in a dimensionless cooling timescale for surface cooling,

$$\beta_{\mathrm{surf}} = \frac{e}{|Q_{\mathrm{cool}}|} \Omega_{\mathrm{K}}, \quad Q_{\mathrm{cool}} = -2\sigma_{\mathrm{SB}} \frac{T^4}{\tau_{\mathrm{eff}}} \quad \tau_{\mathrm{eff}} = \frac{3\tau}{8} + \frac{\sqrt{3}}{4} + \frac{1}{4\tau}, \tag{5}$$

where σ_{SB} denotes the Boltzmann constant and the effective optical depth τ_{eff} follows Hubeny (1990). Defining a timescale for mid-plane cooling is more difficult since the diffusion length l_{d} is not constant. Miranda & Rafikov 2020a show that if we thermally perturb the disc, we can approximate the m-th azimuthal Fourier component of this perturbation. Combining this approximation with the assumption that the dominant diffusion length l_{d} is on the order of H (Ziampras et al. 2023) results in

$$\beta_{\mathrm{mid}} = \frac{\Omega_{\mathrm{K}}}{\eta} \left(H^2 + \frac{1}{3} l_{\mathrm{rad}}^2 \right). \tag{6}$$

We define $l_{\mathrm{rad}} = 1/(\kappa\rho)$, with the opacity given by κ. Combining Eq. 5 and Eq. 6 produces a β-cooling description of FLD:

$$\beta_{\mathrm{fld}} = \frac{\beta_{\mathrm{surf}}}{1 + f}, \quad f = \frac{\beta_{\mathrm{surf}}}{\beta_{\mathrm{mid}}} = 16\pi \frac{\tau_{\mathrm{eff}}}{\tau_{\mathrm{R}}} \frac{\tau_{\mathrm{P}}^2}{6\tau_{\mathrm{P}}^2 + \pi}. \tag{7}$$

We assume that $\tau_{\mathrm{R}} = \tau_{\mathrm{P}}$, where τ_{R} is the Rosseland mean optical depth and τ_{P} is the Planck mean optical depth. In contrast to a full radiative description, $\beta_{\rm fld}$ cools the disc only locally. Ziampras et al. (2023) show that $\beta_{\rm fld}$ can substitute full FLD with respect to the cooling time in shock-driven gap opening, but it cannot reproduce all migration-related effects of FLD (Ziampras et al. 2024). With this, we define three different equations of state, adjusting the complexity of them step-wise:

1. Locally isothermal: there is no compressive heating and the disc is in thermal equilibrium. The temperature is given by a balance between irradiation and surface cooling following Menou & Goodman (2004):

$$T(R) = 18.07\,\mathrm{K}\left(\frac{R}{50\,\mathrm{au}}\right)^{-3/7} \Rightarrow\; h(R) = 0.06\left(\frac{R}{50\,\mathrm{au}}\right)^{2/7}. \tag{8}$$

   With $c_{\rm s} \propto \sqrt{T}$, the pressure is directly linked to the surface density.

2. Constant $\beta = 1$: the system exponentially cools back to the steady-state temperature profile given by Eq. 8 and is only heated by shocks, as in Eq. (3).

3. Adaptive β: the cooling timescale instead follows a density-, temperature-, and opacity-dependent formulation through Eqs. (5)–(7). This represents an accurate model of β following Miranda & Rafikov (2020a); Ziampras et al. (2023); Ziampras et al. (2026). Figure 1 shows $\beta_{\rm fld}$ over the disc extent for our setup at $t = 0$ kyr.

We set $\beta = 1$ for the constant β-cooling simulation, since it translates to strong radiative damping of planetary wakes and therefore to a single-gap configuration (Miranda & Rafikov 2020b; Ziampras et al. 2023; Zhang et al. 2024). This minimises the risk of secondary gaps produced by the planet (Zhang et al. 2018) affecting its inward migration track, but does not necessarily eliminate it (e.g. Lega et al. 2021; Wafflard-Fernandez & Lesur 2025). As shown by Ziampras et al. (2024), radiative processes can modify the local vortensity ϖ through baroclinic forcing $\mathcal{S}$:

$$\frac{\partial\varpi}{\partial t} + (\boldsymbol{v}\cdot\nabla)\,\varpi = \frac{\nabla\Sigma\times\nabla P}{\Sigma^3} = \frac{P}{TR\Sigma^3}\left(\frac{\partial\Sigma}{\partial R}\frac{\partial T}{\partial\phi} - \frac{\partial\Sigma}{\partial\phi}\frac{\partial T}{\partial R}\right) = \mathcal{S}. \tag{9}$$

Specifically, a parcel of gas approaching the planet within the horseshoe region gains (loses) vortensity as it U-turns behind (ahead of) the planet. Cooling results in an asymmetry between the two sides and typically leads to vortensity growth within the planet's horseshoe region, with the effect maximised for $\beta \sim 1$. This can substantially influence the planet's migration, as we discuss in the following. We note that using $\beta_{\rm mid}$ as a substitute for in-plane diffusion can exaggerate this effect (Ziampras et al. 2024), however, we chose to use this approach due to the prohibitive computational costs of a fully radiative model.

2.2. Numerical setup

We used the hydrodynamic code `FARGOCPT` (Rometsch et al. 2024), a successor of `Fargo` (Masset 2000), to create a vertically integrated, cylindrically symmetric (R, ϕ) disc extending from 5–500 au. We analysed the data using `python`. We set the grids resolution to 16 cells per scale height at 50 au in radial and azimuthal directions. This corresponds to 1230×1676 approximately square cells, logarithmically spaced in the radial direction. The inner and outer boundaries are set to outflow, both with damping zones in front of them. These damping zones range from 5–6 au and 425–500 au, respectively, damping the values exponentially on a timescale of $10^{-1}\,2\pi/\Omega_{\rm K}$ evaluated at the boundary. We tested different configurations of boundary conditions, damping zones, and exponential cut-off beforehand. The chosen setup prevented any pile-ups at the inner boundary and reflections of density waves at the outer boundary. We set the initial surface density to

$$\Sigma = 10\,\frac{\mathrm{g}}{\mathrm{cm}^2}\cdot\left(\frac{R}{50\,\mathrm{au}}\right)^{-1} C_{\rm o}(r). \tag{10}$$

An outer surface-density profile cut-off is given by $C_{\rm o}(r)$, implemented starting at 350 au:

$$C_{\rm o} = \left(1 + \exp\left(\frac{(-(r - r_{\rm oC}))}{w_{\rm oC}}\right)\right)^{-1}. \tag{11}$$

Here, $r_{\rm oC} = 350$ au is the cut-off point and $w_{\rm oC} = 35$ au the cut-off width. The total disc mass between 5–500 au is $\approx 0.12\,\mathrm{M}_\odot$. We disabled gas self-gravity, since the Toomre parameter $Q = \frac{c_s\Omega_{\rm K}}{\pi G\Sigma} > 1$ over the entire disc. We used a turbulent α-value of $\alpha = 10^{-4}$ for our viscosity. The disc aspect ratio follows Eq. (8). The central star has solar parameters, and the grid frame is centred on the star. All disc parameters fall within the range characteristic of DSHARP discs, except for the radial extent (Dullemond et al. 2018; Huang et al. 2018; Zhang et al. 2025). We set the planet mass $M_{\rm p} = 100\,\mathrm{M}_\oplus$. We define the thermal mass as

$$M_{\rm th} = 2\frac{h_{\rm p}^3}{3}M_*, \tag{12}$$

and the feedback mass as

$$M_{\rm f} \approx 3.8\left(\frac{Q}{h}\right)^{-5/13} M_{\rm th}. \tag{13}$$

If $M_{\rm p} \approx M_{\rm th}$, the planetary wakes steepen into shock waves immediately after launch, while a planet with $M_{\rm p} \approx M_{\rm f}$ has the minimal mass required to significantly modify its surroundings. Mc19 and Z25 define different migration regimes based on the ratios of $M_{\rm p}$ to $M_{\rm th}$ and $M_{\rm p}$ to $M_{\rm f}$. In this paper $M_{\rm p} \approx 2\,M_{\rm th}$ and $\approx 3.4\,M_{\rm f}$. We placed the planet at $R_{\rm p} = 50$ au and allowed it to migrate immediately. The planet's potential is given by

$$\Phi_{\rm p,2D} = -\frac{\mathrm{G}M_{\rm p}}{\sqrt{d^2 + s^2}}, \quad \boldsymbol{d} = \boldsymbol{R} - \boldsymbol{R}_{\rm p}\,, \tag{14}$$

with a smoothing length $s = \epsilon H$ and a smoothing parameter $\epsilon = 0.6$to account for the vertical stratification of the disc (Müller & Kley 2012). We let the system evolve for 530 kyr, corresponding to 1500 orbits at $R = 50$ au.

The planet and star influence each other's motion. Because we fixed our frame onto the star, the frame is non-inertial, introducing additional forces. In `FARGOCPT`, these forces are accounted for by the so-called indirect terms. We include the indirect acceleration of the star due to the star–planet system orbiting their common centre of mass. However, because we did not include self-gravity in our simulations, we disabled the disc-disc indirect term 'ITdd' described in Crida et al. (2025b) (i.e. the back-reaction of the disc's acceleration on the star onto the disc), which would otherwise artificially enhance vortices and potentially trigger the reflex instability (Crida et al. 2025a).

We also included dust in our simulation. In `FARGOCPT`, this is achieved using Lagrangian super-particles with a particle density of 2.08 g/cm^3 following the DIANA standard model. They

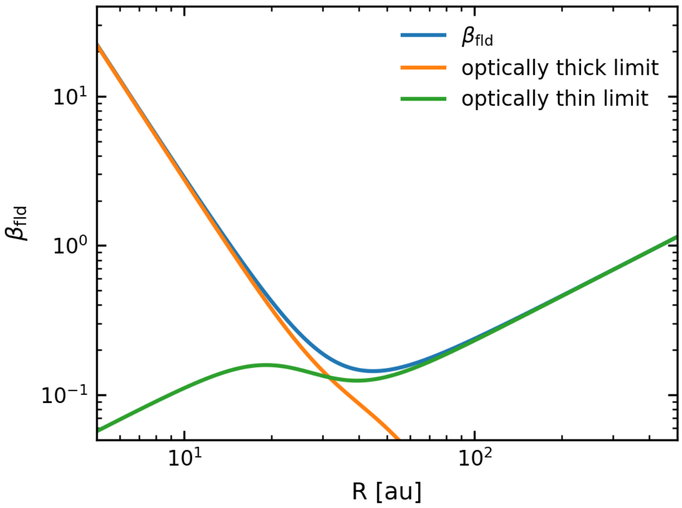

Fig. 1: Dimensionless cooling timescale $\beta_{\rm fld}$ across the extend of the disc at $t = 0$ kyr. We also plot the approximations for the optically thick and optically thin limit.

Table 1: Overview of the simulations considered in this study.

Name	EOS	$M_{\rm p}$ [$\mathrm{M}_\oplus$]
`iso`	isothermal	100
`beta-01`	$\beta = 0.01$	100
`beta`	$\beta = 1$	100
`beta-3`	$\beta = 3$	100
`beta-7.5`	$\beta = 7.5$	100
`adapt`	$\beta = \beta_{\rm fld}$	100
`adapt-low-mass`	$\beta = \beta_{\rm fld}$	62

are split into three sets of 33 000 particles with sizes $a_{\rm d}$ fixed at 3 μm, 30 μm, and 0.3 mm. These sizes correspond to Stokes numbers of St = 10^{-4}, 10^{-3}, and 10^{-2} at 50 au, respectively. Their surface density profile follows the gas surface density without the cut-off. The initial dust-to-gas ratio is 0.01, and the total dust mass is therefore 0.0012 $\mathrm{M}_\odot$, initialised with an MRN ((Mathis et al. 1977a)) size distribution such that $\Sigma_{{\rm d},i} \propto a_{{\rm d},i}^{0.5}$ (Mathis et al. 1977b). We did not include dust feedback onto the gas.

Table 1 lists the simulations. We analyse the migration of some simulations in detail in Sect. 3.2 and discuss their post-processing in Sect. 3.3.

3. Results

3.1. Migration regimes

One aspect of the simulation analysis is the identification of the planet's migration regimes and their link to the feedback and thermal masses $M_{\rm f}$, $M_{\rm th}$ (see Eqs. (12) and (13)). Mc19 and Z25 demonstrated that in nearly inviscid discs, planets with masses $M_{\rm f} \lesssim M_{\rm p} \lesssim M_{\rm th}$ migrate in the turbulent vortex-assisted regime. The planet opens a partial asymmetric gap that is deeper behind the planet than ahead of it, resulting in a pronounced surface-density gradient at the outer gap edge (see also Fig. 5 in Z25). This configuration is eventually unstable to the Rossby wave instability (RWI; Lovelace et al. 1999) and is further subject to baroclinic forcing via radiative processes that can significantly modify the vortensity around the planet's orbit (Ziampras et al. 2024, 2025b). The change in vortensity is directly linked to a change in the surface-density profile, which produces additional RWI vortices. These RWI vortices, whether driven by baroclinic forcing or not, at the outer gap edge refill the gap and thus sustain the outer Lindblad torques (Armitage & Kley 2019), driving inward migration. With a width of ∼ 6–23% of the half-width of the horseshoe region, these small vortices are often only visible when inspecting the inverse vortensity ($\mathcal{IV}$) profile at high resolution. They can also be identified by plotting the relative deviation from the azimuthally averaged inverse vortensity, $\mathcal{IV}/\overline{\mathcal{IV}} - 1$. We do not distinguish between two vortex-assisted sub-regimes, one without cooling and one with cooling, but note that when cooling is active, baroclinic forcing significantly alters the regime.

As $M_{\rm th}$ decreases while the planet migrates inwards, the planet mass eventually becomes super-thermal and transitions into the type-II regime, ultimately stalling its migration.

In addition, we observe intermittent migration, first introduced by Mc19 (see also WB20; Z25; M26). Intermittent migration can be described as brief episodes of type-III migration (Masset & Papaloizou 2003), in which the dynamical co-rotation on the planet (Paardekooper 2014),

$$\Gamma_{\rm h} = 2\pi\left(1 - \frac{\mathcal{IV}_{\rm h}}{\mathcal{IV}_{\rm p}}\right)\Sigma_{\rm p} R_{\rm p}^2 x_{\rm h} \Omega_{\rm p}\left(\frac{{\rm d}R_{\rm p}}{{\rm d}t} - u_R\right), \quad (15)$$

becomes momentarily strongly negative due to a sharp contrast between the $\mathcal{IV}$ enclosed within the horseshoe region ($\mathcal{IV}_{\rm h}$) and the local, approximately Keplerian, $\mathcal{IV}$ ($\approx 2\Omega_{\rm K}^{-1}$). This process can be repeated several times. In the above equation, $x_{\rm h}$ denotes the half-width of the horseshoe region (Paardekooper et al. 2010), u_R is the local radial velocity of the disc, and quantities with a subscript 'p' are evaluated at the planet's location.

Generally, intermittent migration can be further divided into the following phases, which we illustrate using our fiducial model `iso` (Fig. 2). In our models intermittent migration differs slightly from those described in WB20, in particular, as we find that vortex formation is triggered after a jump, more in line with the description of M26.

a) First, due to gap opening by the planet, an $\mathcal{IV}$ maximum forms ahead of the planet ($R < R_{\rm p}$) and an $\mathcal{IV}$ minimum behind it ($R > R_{\rm p}$).
b) The minimum and maximum migrate inwards together with the planet. In this paper, the planet migrates in the vortex-assisted regime.
c) The planet's migration is accelerated by small RWI vortices at the outer gap edge. This acceleration enables the planet to catch up with the $\mathcal{IV}$ structures it has generated, which in turn triggers a short episode of runaway migration. All material in the $\mathcal{IV}$ maximum ahead of the planet then enters the horseshoe region, performs U-turns, and accelerates migration (see Eq. 15), breaking into small vortices during this process.
d) This runaway phase ends when all material initially in the $\mathcal{IV}$ maximum ahead of the planet has entered the horseshoe region. After the jump, the planet's semi-major axis fluctuates for a short duration due to the small vortices created during the jump.

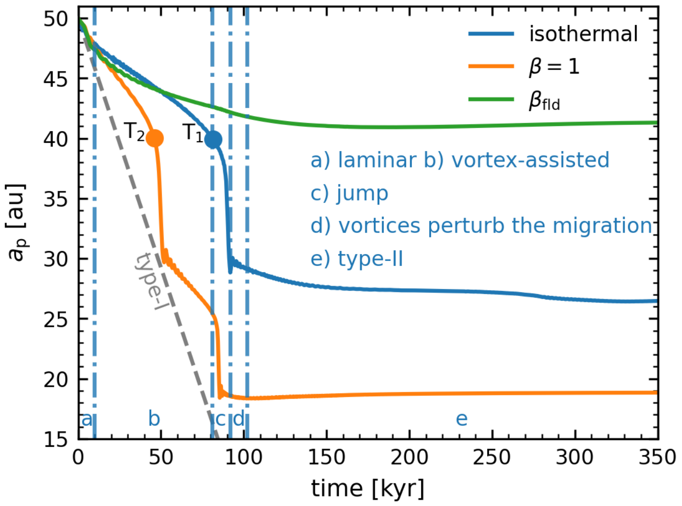

Fig. 2: Semi-major axis (a_p) evolution of models `iso`, `beta`, and `adapt`. Figure 6 shows the inverse vortensity at T_1 and T_2. The dash-dotted lines indicate the different stages of the migration of model `iso`. The plot is truncated at 350 kyr because the planet's semi-major axis does not change significantly thereafter.

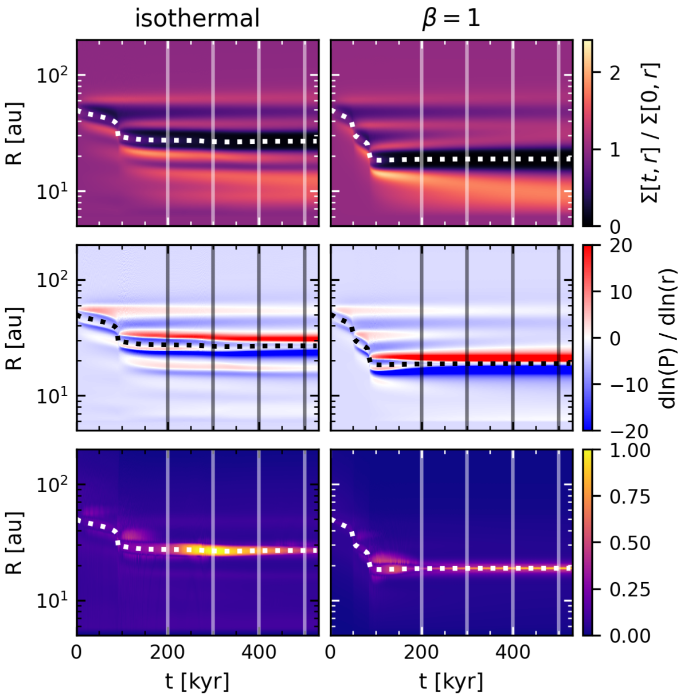

Fig. 3: Averaged surface density (top), azimuthally averaged values $dln(P)/dln(r)$ (centre), and standard deviation of Σ in the azimuthal direction, normalised to show asymmetries in Σ (bottom), for models `iso` (left) and `beta` (right) over the span of the whole disc and the duration of the simulation. In the centre panels, white regions at the transition from red to blue (towards larger R) indicate local pressure maxima. Transition from blue to red (towards larger R) indicate local pressure minima. Light pink regions in the bottom panels indicate large-scale vortices. Values within the horseshoe region cannot be correctly plotted and should be ignored. Dotted lines show the planet's semi-major axis. Vertical lines indicate the times at which we plot the convolved intensity profile in Fig. 14.

3.2. Planetary migration

This section provides an evaluation of the migration behaviour of each simulation listed in Tab. 1. We then analyse the post-processed intensity profiles in Sect. 3.3.

3.2.1. Isothermal model

First, we analyse the simulation with the most simplified equation of state (EOS): `iso`. This simulation confirms the results of M26, Mc19, and WB20 and serves as the fiducial model of this paper.

Fig. 2 shows the evolution of the semi-major axis of the planet. The planet starts its migration in the classical type-I regime for a very short period of time, ~ 3 kyr, during which no significant gap opens. It then transitions into the feedback regime and slows down. Shortly after, the planet enters the vortex-assisted regime, partially accelerating its migration again. Around $t \sim 81$ kyr, the planet undergoes a migration jump as described in Mc19. After the jump, at $R_p \approx 26$ au, the planet transitions to the type-II regime, carving a substantially deeper gap as it becomes significantly super-thermal, with $M_p = 3.4\,M_{th}$ at this radial location (Z25). Around $t = 320$ kyr, the planet transitions to slow outward migration.

The migration jump and the planet's ability to open a gap create pressure maxima and minima in the disc (Mc19, WB20), which act as dust traps (Pinilla et al. 2012). The centre-left panel in Fig. 3 shows the azimuthally averaged radial pressure gradient for the model `iso`, where P is the vertically integrated pressure. We observe three distinct pressure maxima ($R_{max} \approx 60$, 37, and 20 au) and four additional minima ($R_{min} \approx 48$, 32, 25, and 17 au). The planet-induced density variation causes a corresponding change in pressure, shifting the pressure maxima to the locations of the density maxima (Goldreich & Tremaine 1979; Crida et al. 2006). Therefore, the pressure minima coincide with the gaps carved by the planet. Here, the minima at $R_{min} \approx 32$ and 25 au lie within the planet's primary gap. The pressure maxima coincide with the rings (Fig. 4).

As seen in M26, large scale vortices form but have a very short lifetime. Fig. 5 illustrates their appearance in the $\mathcal{IV}$ profile. We detect three large-scale (~ 8 au radial extend) vortices, which appear as local maxima in the $\mathcal{IV}$ profile. Over the next 10 kyr, these three vortices merge into a single vortex, which dissipates after 100 kyr (Fig. 3). We observe an additional large-scale vortex created after the migration jump between 40–30 au, at $R \approx 37$ au, with a lifetime of $\sim$90 kyr. Both vortices are fully decoupled from the planet. They eventually smear out azimuthally, forming rings of low vortensity and, importantly, preserving the underlying pressure maxima.

The gap at $R \approx 48$ au is carved by the planet during its slow inward migration up to $t \sim 81$ kyr. Even after the migration jump, the initial primary gap and resulting pressure profile dissipate slowly due to the low viscosity and remain visible in the gas surface density profile at $t = 500$ kyr. Figures 3 and 4 additionally show that the planet carves a secondary gap at $R_{max} \approx 17$ au. This gap is created by shocks from the secondary and tertiary spirals launched by the planet (Bae & Zhu 2018a,b) and has been observed by Zhang et al. (2024) and M26.

While the gas surface-density profile and dust-particle distribution share the same features, these features appear amplified in the dust (Fig. 4). This includes material at the co-orbital Lagrange point L5, which is not visible in the gas surface-density

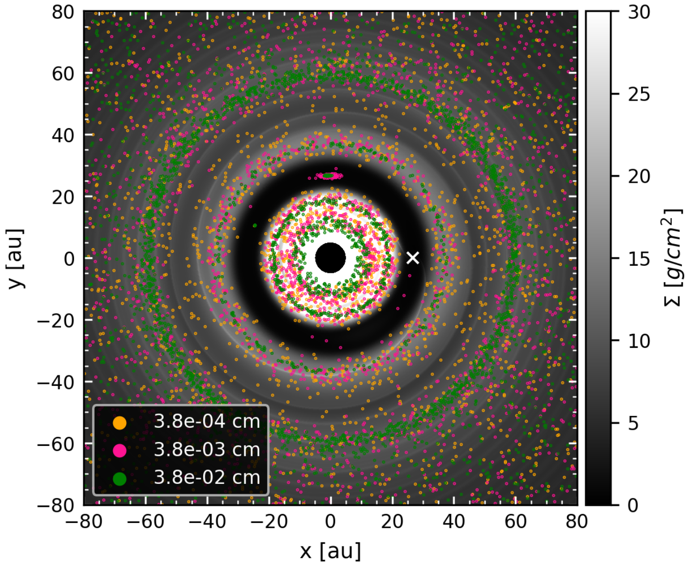

Fig. 4: Surface density profile of model `iso` at $t = 500\,$kyr. The inset shows which colours correspond to the respective particle sizes.

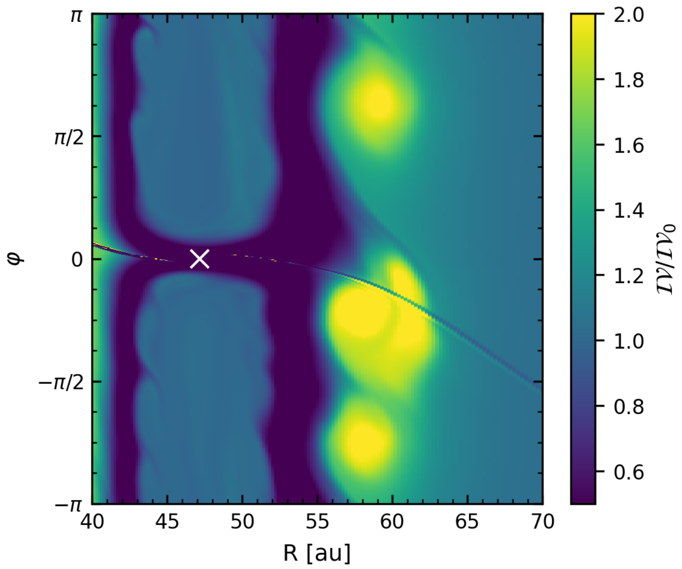

Fig. 5: Normalized inverse vortensity of model `iso` at $t \approx 14\,$kyr. The quantity $\mathcal{IV}_0$ denotes the initial inverse vortensity of the disc. Three large-scale vortices are visible around $R = 60\,$au. The white cross marks the planet's location.

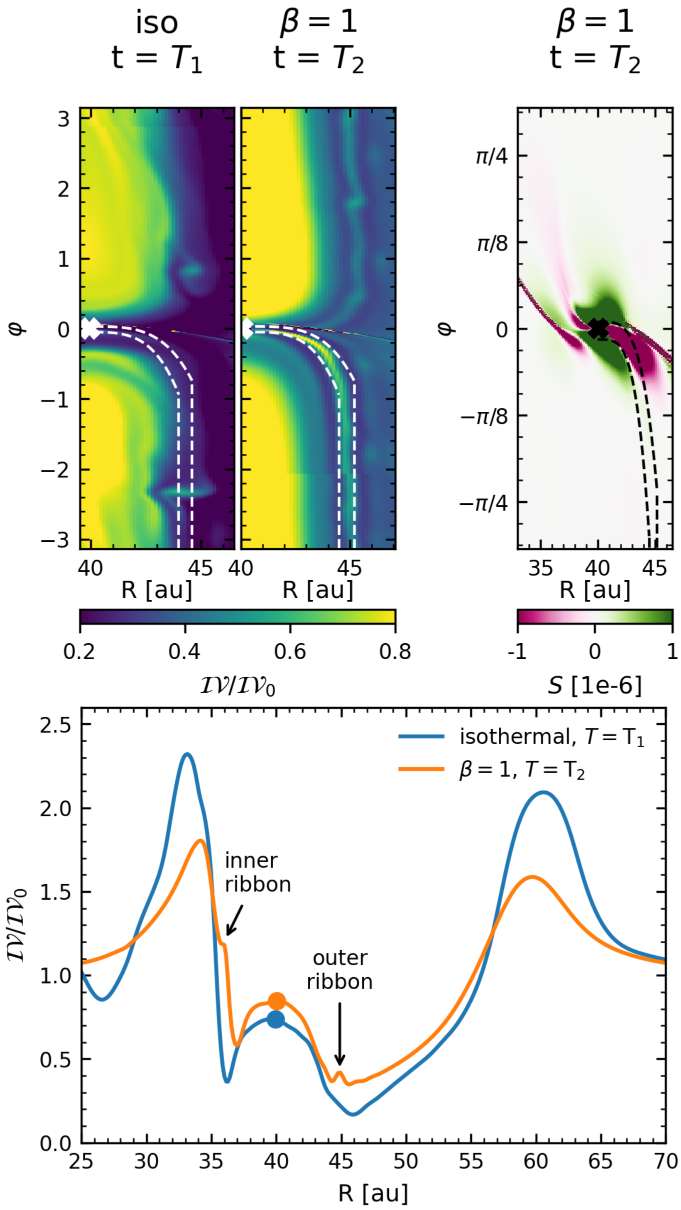

Fig. 6: Small-scale vortices at the outer horseshoe edge of model `iso` (left) and model `beta` (centre) during migration in the vortex-assisted regimes. Right: Baroclinic forcing (in cgs units) of model `beta` in the vicinity of the planet. The quantity $\mathcal{IV}_0$ denotes the initial inverse vortensity of the disc. Without baroclinic forcing, they appear as maxima in the $\mathcal{IV}$ profile around $R \approx 44.5$ au. With baroclinic forcing, we observe 'ribbons' of high and low $\mathcal{IV}$, where high-$\mathcal{IV}$ material breaks into vortices around $R \approx 46.5$ au. These structures are indicated by dotted lines. We also observe an asymmetry in the baroclinic forcing term. The white and black crosses marks the planet's position. Bottom: Averaged $\mathcal{IV}$ profiles at the same points in time.

profile. We further observe that the outer ring is predominantly composed of faster-drifting 0.3 mm-sized particles that are not located within the gaps, whereas smaller particles follow the gas across pressure maxima (Weidenschilling 1977; Nakagawa et al. 1986; Zhang et al. 2018).

3.2.2. Constant β

We now introduce cooling with a constant cooling timescale $\beta = 1$. Fig. 2 shows the semi-major axis evolution of model `beta`. The planet starts carving a gap, producing the same $\mathcal{IV}$ minima and maxima structures as in model `iso`. In addition to the Rossby-wave unstable partial gap, cooling drives significant baroclinic forcing at the gap edges (Z25). The asymmetric baroclinic forcing profile produces three ribbons of high and low $\mathcal{IV}$ at the outer horseshoe edge, shown in the right panel of Fig. 6, as opposed to model `iso` (left panel of the same figure). Further analysis (see also Appendix B) shows that these ribbons are created by gas outside the horseshoe orbit interacting with the planetary shocks. Figure 7 shows a schematic sketch of the contribution term $\partial\Sigma/\partial R \cdot \partial T/\partial\phi$ of the baroclinic forcing term $\mathcal{S}$ (Eq. (9)) in the red-outlined area. The planet accumulates mass

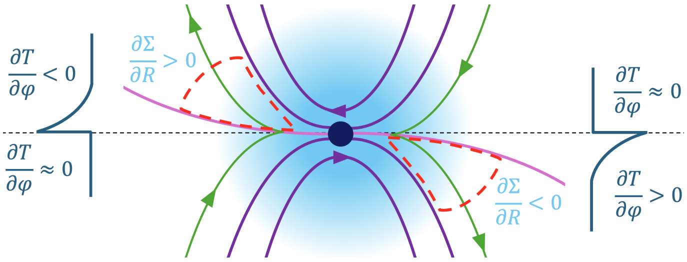

Fig. 7: Schematic illustration explaining the baroclinic forcing contribution which creates the 'ribbon' of high $\mathcal{IV}$ in model `beta`, as shown in Fig. 6. Its shows the planet (dark blue dot), the orbiting material in the horseshoe region (purple), the spirals created by the planet (pink), and the unbound material (green). The red-outlined areas highlight the regions of negative baroclinic forcing.

around its Hill sphere, which determines $\partial\Sigma/\partial R$. Meanwhile, unbound gas outside the horseshoe orbits is heated by the planetary shock and subsequently cools, determining $\partial T/\partial\phi$. Combining both terms results in a negative baroclinic forcing contribution, which produces the low vortensity ribbon in model `beta`. For an isothermal EOS, $\partial T/\partial\phi = 0$, setting this baroclinic forcing contribution to 0. The baroclinic forcing acts as a very efficient vortensity 'sink', to the point that the gradient relative to the background becomes large enough for the flow to quickly break into vortices. These vortices refill the outer gap faster than those seen in the `iso` model. Additionally, the term $\partial\Sigma/\partial\phi \cdot \partial T/\partial R$ in the baroclinic forcing drives vortensity inside the horseshoe region and thus contributes to inward migration, as in Ziampras et al. (2024). This is further discussed in Appendix B.

The planet migrates in the vortex-assisted regime and undergoes its first intermittent migration jump at $t \sim 46$ kyr. At this time, the planet is located at $R_p = 40$ au, the same radius at which model `iso` enters the intermittent migration. In both simulations, the planet ends the migration jump at $R_p \approx 30$ au. Whether and when the planet undergoes a jump is determined by its ability to catch up with its own gap structure. The structure of the gaps depends on the shock distance, which is proportional to c_s (Goodman & Rafikov 2001). Miranda & Rafikov (2020b) determined an effective c_s, which is very close to the isothermal sound speed for $\beta = 1$. Therefore, we expect that both planets open a similar gap, which is confirmed by Fig. 8. Figures 4 and 5 in Ziampras et al. (2026) also show that the angular-momentum deposited in the gap is similar for isothermal and $\beta = 1$ simulations. Model `beta` presents a shallower gap, because it was plotted at an earlier time ($T_1 > T_2$).

The planet re-enters the vortex-assisted regime after the first jump and carves a deeper gap than before the jump. The process repeats: the planet modifies its surroundings to create a new $\mathcal{IV}$ minimum and maximum around it, and the RWI vortices remain strong enough to significantly refill the now deeper primary gap, maintaining the inward migration. As a result, the planet undergoes a second intermittent migration jump at $t = 82$ kyr, covering another 6.6 au in 4 kyr.

After the second jump, the planet reaches the type-II regime and migrates outward slowly from $R_p \approx 18$ au. Here, $M_p = 4.49\,M_{th}$, and the planet mass is super-thermal, as expected (Ziampras et al. 2025b). The planet's primary gap depth decreases rapidly, which is expected, since the primary gap opening is most efficient for $\beta = 1$ (Miranda & Rafikov (2020b)).

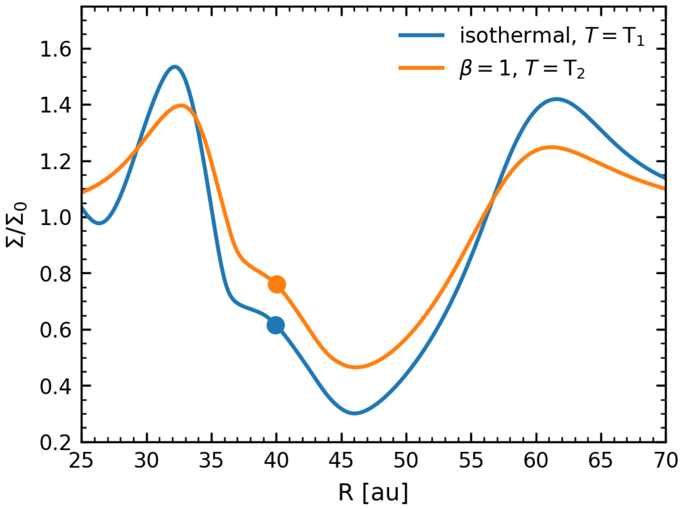

Fig. 8: Normalized, azimuthally averaged gas surface density profile of models `iso` and `beta` at $t = T_1$ and T_2. The dot indicates the planet's position.

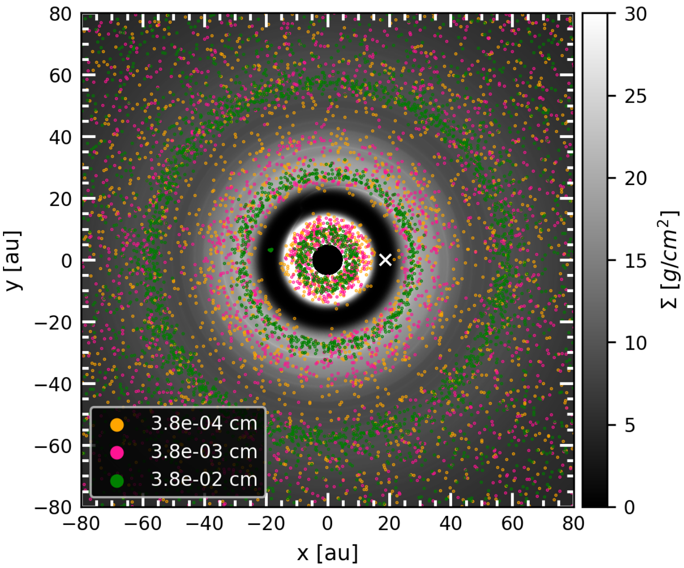

Fig. 9: Surface density profile with dust for model `beta` at $t = 500$ kyr. The inset shows which colours correspond to the respective particle sizes.

We observe that the pressure maxima created by the planet at $R_{max} = 37$ au and $R_{max} = 24$ au begin to overlap around $t \sim 300$ kyr, since the gap edge at $R = 24$ au shifts towards higher radii (Fig. 3). Therefore, the gas surface density and particle distribution in Fig. 9 show only the outermost and innermost rings ($R_{max} \approx 60$ and 28 au) and gaps ($R_{min} \approx 47$ au and 18 au), even though the planet undergoes two intermittent migration phases. Similar to model `iso`, the dust distribution shows similar but more pronounced features compared to the gas surface density, with larger grains populating the rings. No secondary gap is opened interior to the planet's orbit, as expected for $\beta = 1$ (Fig. 3).

During the first jump, when the planet moves from 40 au down to 30 au, a large vortex forms around $R \approx 35$ au, with a lifetime of ~ 50 kyr, which is not coupled to the planet. The second jump (the planet moves from 25 au to 18 au) generates two large-scale vortices at $R \approx 24$ au and $R \approx 16$ au. All three exhibit the

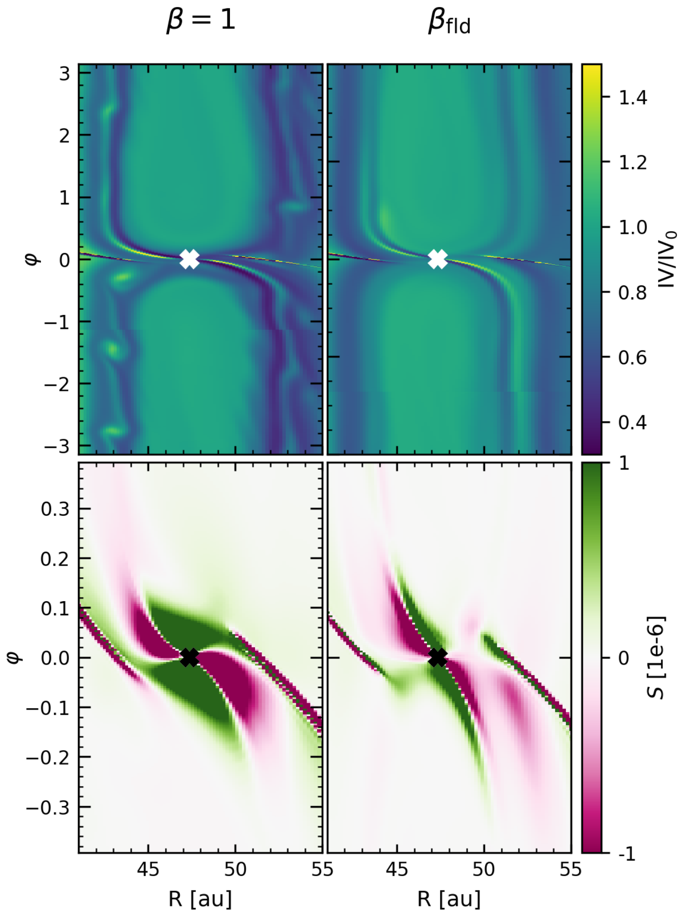

Fig. 10: Normalized inverse vortensity profile and baroclinic forcing S (in cgs units) in the horseshoe region of models `beta` (left) and `adapt` (right) at $t \approx 10$ kyr. Although both simulations include cooling, model `beta` exhibits a significantly more asymmetric baroclinic forcing term , which produces the characteristic ribbons of high and low $\mathcal{IV}$, which break into vortices. The more symmetric baroclinic forcing in `adapt` does not produce this $\mathcal{IV}$ structure. The white cross marks the planet's position.

same $\mathcal{IV}$ structure as the vortex in Fig. 5 . While the vortex at $R \approx 16$ au only has a lifetime of ~ 30 kyr, the vortex at $R \approx 24$ au survives significantly longer, for 90 kyr. The latter may be periodically perturbed by the planet, which delays its dissipation.

3.2.3. Adaptive β

Next, we introduce an adaptive cooling timescale $\beta_{\rm fld}$, the model closest to the full radiative disc description. Fig. 2 shows the semi-major axis evolution of model `adapt`. After opening a sufficiently deep gap, the planet initially migrates in a type-I like regime, with a starting value of $\beta_{\rm fld} \approx 0.15$. The disc structure changes, creating an $\mathcal{IV}$ maximum ahead of the planet and a minimum behind it.

After 10 kyr, this changes, and the planet enters the vortex-assisted regime with an asymmetric baroclinic forcing term. Baroclinic forcing is much weaker than in the $\beta = 1$ case, with only small, sometimes barely visible vortices in the $\mathcal{IV}$ profile (Fig. 10). Additionally, the baroclinic forcing term becomes asymmetric only once the planet has already opened a significant gap. Both effects together result in slow migration, and the planet does not catch up with the created $\mathcal{IV}$ structures. Hence,

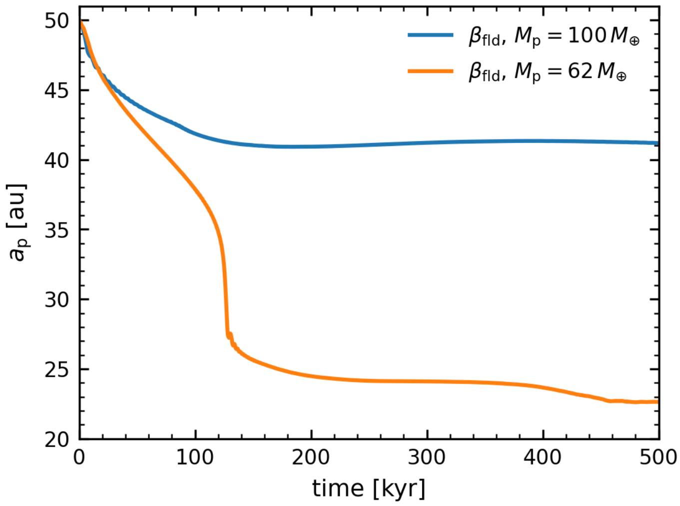

Fig. 11: Semi-major axis ($a_{\rm p}$) evolution of models `adapt-low-mass` and `adapt`.

the planet does not undergo a migration jump. We observe an additional negative baroclinic forcing feature at $R \approx 52$ au in model `adapt`, likely caused by the stronger temperature dependence of $\beta_{\rm fld}$.

At $t \sim 180$ kyr, $R_p \sim 41$ au, the planet enters the type-II regime but migrates outward. At this point, $M_{\rm p} = 2.4 M_{\rm th}$ and $\beta_{\rm fld}$ has an approximate value of $\beta_{\rm fld} \approx 0.146$, which is close to the starting value. We observe no large-scale vortices over the duration of the simulation.

Although $\beta_{\rm fld}$ varies across the disc, the planet halts its migration in the transition between the optically thin and optically thick disc regimes, where the dependence on Σ is weak (Fig. 1) and does not trigger a runaway process. Even though the planet stalls its migration, baroclinic forcing continues to increase in strength due to the descending gap depth and the increasing steepness of the gap edge. At $t \sim 450$ kyr the small-scale vortices produced by baroclinic forcing become strong enough to appear in the $\mathcal{IV}$ profile (Fig. 6, centre plot) and the planet could soon re-enter the vortex-assisted regime. This is supported by the migration track, which now no longer follows a smooth curve, but fluctuates.

Nevertheless, the planet did not undergo intermittent migration in this simulation; consequently, only the primary and secondary gaps carved by the planet are present. Since this work focuses on planets that experience migration jumps and on their resulting structures, we reduced the planet mass from $M_{\rm p} = 100\,{\rm M}_\oplus$ to $M_{\rm p} = 62\,{\rm M}_\oplus$, corresponding to $M_{\rm p} \approx 1.3 M_{\rm th}$. We name this new simulation `adapt-low-mass`. While we expect the migration behaviour to change, we note that $\beta_{\rm fld}$ does not depend on the planet's mass, enabling a fair comparison between the two models.

3.2.4. Adaptive β with a lower-mass planet

Fig. 11 shows the semi-major axis evolution of model `adapt-low-mass`. The simulation undergoes an intermittent migration jump. As in model `adapt`, `adapt-low-mass` starts its migration in the laminar regime and switches to vortex-assisted migration after 15 kyr. Initially, small vortices at the outer gap edge are only visible when plotting the deviation from the azimuthally averaged $\mathcal{IV}$ profile, and later they also appear in the $\mathcal{IV}$ profile, as seen in Fig. 6 (left panel). At later times, we observe the ribbons of high and low $\mathcal{IV}$ (Fig. 6, centre panel),

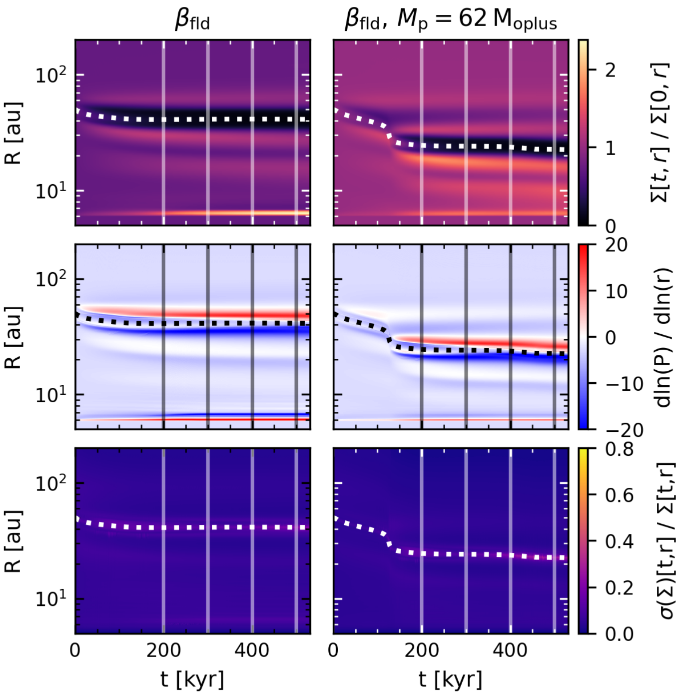

Fig. 12: Averaged surface density (top), azimuthally averaged values $dln(P)/dln(r)$ (centre), and asymmetries in Σ (bottom) of models `adapt` (left) and `adapt-low-mass` (right) over the span of the whole disc and the duration of the simulation. Due to the variable cooling timescale, a temperature spike forms in front of the inner damping zone. This does not influence the planet's migration.

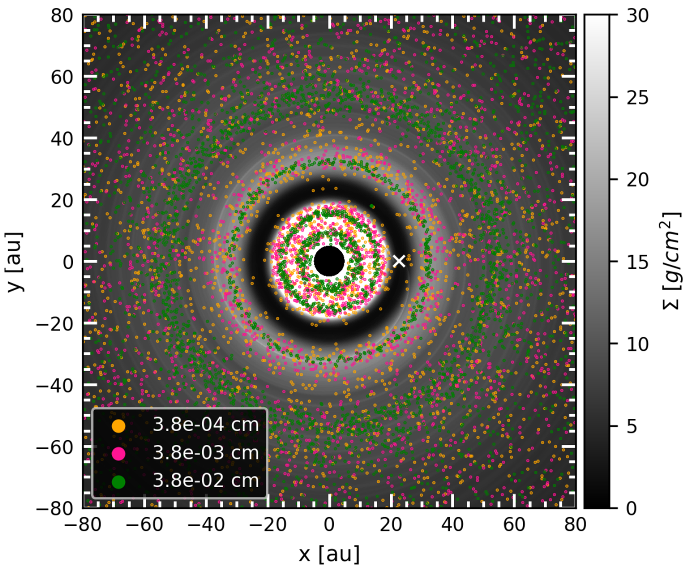

Fig. 13: Surface density profile with dust for model `adapt-low-mass` at $t = 500$ kyr. The inset shows which colours correspond to the respective particle sizes.

characteristic of strong baroclinic forcing. We conclude that the planet is in the vortex-assisted regime, primarily driven by baroclinic forcing. These vortices accelerate the planet sufficiently to trigger a migration jump around $t = 120$ kyr, covering 7.5 au in 9 kyr. The planet reaches an equilibrium at $R_{\rm p} \approx 24$ au and migrates in the type-II regime, with $M_{\rm p} = 2.24 M_{\rm th}$. There, the cooling timescale assumes a value of $\beta_{\rm fld} = 0.28$.

Unlike `adapt`, the planet migrated far enough into the optically thick regime of the disc, where $\beta_{\rm fld}$ depends strongly on Σ (Fig. 1). Hence, the planet enters a runaway process as described in Sect. 3.1, reducing its surface density by a factor of 100 over the next 300 kyr. Meanwhile, small vortices form at the outer gap edge (as shown in Fig. 6, left panel), likely driven by a combination of the sharp radial vortensity contrast from gap opening and baroclinic forcing, as in model `adapt`. However, since the gap is continuously cleared, the planet remains in the type-II regime until the end of the simulation.

The planet carves three gaps ($R_{\rm min} \approx 45$, 24, and 13 au) and three rings ($R_{\rm max} \approx 60$, 33, and 18 au) consistent with the pressure profile. The pressure maxima and minima associated with the innermost gap and ring, caused by the planet's secondary gap, are significantly less pronounced (Fig. 12). Nevertheless, they remain sharp enough to produce visible gaps in the averaged surface density profile (Fig. 12) as well as in the dust particle distribution (Fig. 13. The gas and dust distributions are consistent with expectations (Fig. 13).

3.3. Radiative transfer images

To produce images similar to those obtained in the DSHARP survey, we modelled the evolution of dust grains alongside the gas, as described in Sect. 2.2. We then binned the super-particles onto a surface density grid using the `python` module `coord2sigma` (Rometsch 2023). We calculated the observed intensity I_ν as

$$I_\nu = (1 - e^{-\tau_\nu})\, B_\nu. \tag{16}$$

Here, $B_\nu(T)$ denotes the black-body intensity profile evaluated at the gas temperature $T_{\rm gas}$. We used the DIANA standard opacities for each dust species, computed with `optool` (Dominik et al. 2021) at $\lambda \approx 1.25$ mm, the wavelength used by the DSHARP survey and ALMA Band 6. We then interpolated the intensity heat map $I_\nu(R, \phi)$ onto a Cartesian grid and convolved with a Gaussian kernel. We assumed a distance of 100 pc and an inclination of 0° for the discs and adopted the configuration used for Elias 20 in DSHARP, with a beam of angular size $\theta_{\rm b} = 32 \times 23$ mas and a position angle of $\mathrm{PA_b} = 76°$ (Andrews et al. 2018). This produces observation-like images for model `iso`, `beta`, `adapt`, and `adapt-low-mass` (Fig. 14).
Model `iso` displays several ring and gap features over the duration of the simulation. We also observe material at the co-orbital Lagrange points, which is cleared over time (as also seen in Rodenkirch et al. 2021). A small remainder of the dust at the L5 Lagrange point remains visible at 500 kyr. The planet's continuous gap opening and dust drift causes the rings at $R \approx 37$ and 20 au to become brighter as the simulation evolves from $t = 200$ kyr to $t = 500$ kyr. Comparing the convolved intensity profile with the dust distribution in Fig. 4, the gaps are deeper and more pronounced in the dust picture. Nevertheless, all structures are present in both distributions.
Compared to model `iso`, the planet in model `beta` undergoes two migration jumps instead of one. Fig. 3 shows that some pressure maxima merge over the duration of the simulation due to the shift of the gap edge at $R \approx 24$ au. As shown in Fig. 9, this influences the dust particle distribution. Figure 14 also shows the merging of the inner ring and the gap structure, leaving only two distinct gaps at $t = 500$ kyr. We additionally observe that the gap

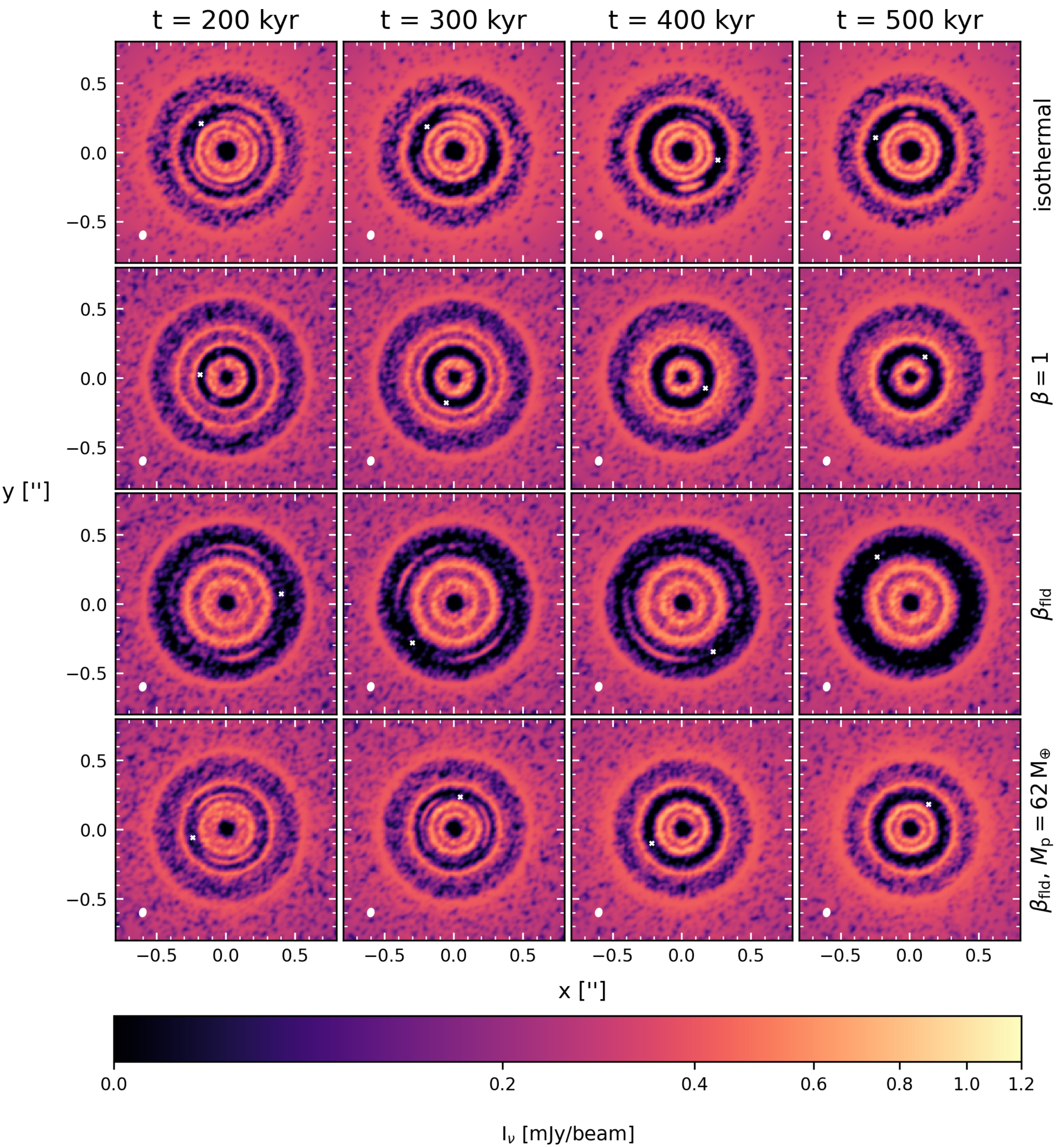

Fig. 14: Intensity I_ν of model `iso`, `beta`, `adapt` and `adapt-low-mass`, convolved with a Gaussian beam at t = 200, 300, 400, and 500 kyr. The white ellipse represents the beam, and the white cross indicates the planet's position.

at the planet's final location is almost cleared at t = 200 kyr, with very little material remaining at the co-orbital Lagrange points. The planet does not open a secondary gap, as expected for $\beta = 1$ (Miranda & Rafikov 2020b; Ziampras et al. 2023; Zhang et al. 2024).

The planet in model `adapt` does not undergo a migration jump; hence, the convolved intensity profiles show only the primary and secondary gap around the planet and interior to its orbit, respectively. Consistent with the other simulations, a substantial accumulation of material is present at the co-orbital Lagrange points, which is progressively cleared by t = 500 kyr.

The intensity profile of `adapt-low-mass` shows three rings and gaps: the two outermost ones are created by the migration jump, while the innermost structures are produced by the planet's secondary gap. The outer two rings remain visible in the intensity profile from their formation until the end of the simulation,

400 kyr later. The innermost ring and gap only become distinguishable at $t = 300$ kyr, over 100 kyr after the planet enters the stalling regime. Although the surface density of the primary gap is drastically reduced (in part due to cooling, e.g. Miranda & Rafikov 2020b), this does not apply to the planet's secondary gap. Unlike in models `iso` and `beta`, there are no large vortices, but model `adapt-low-mass` still creates pressure maxima. Additionally, the gap at the planet's final location ($R_{\min} \approx 24$ au) still contains some dust at the co-orbital Lagrange points up to $t = 350$ kyr, although its surface density decreases rapidly over time. This is due to dust drift. Comparing the particle distribution in Fig. 13 with the intensity profile in Fig. 14, the planet's secondary gap is less visible, while asymmetries in the ring at $R_{\max} = 18$ au become more apparent.
This analysis shows that all three simulations that undergo a migration jump produce observable dust structures, which remain visible over the full duration of the simulations. This suggests that we may be able to explain the dynamical history of some planetary systems that show similar structures to those in our simulations.
We note that the 'noise' in the synthetic observations arises from the binned particle distribution in the simulation output and is unrelated to instrument noise (which would be negligible on this scale). For the same reason, we caution that apparent asymmetries within rings should not be interpreted as actual non-axisymmetric features.

We find that planets in simulations with an isothermal EOS, constant β-cooling, or $\beta_{\rm fld}$ can experience one or several migration jumps. These jumps create pressure maxima and minima in the disc, which act as dust traps that translate into visible rings and gaps in the intensity profile. Most of them remain visible at $t = 500$ kyr. We changed the planet mass in model `adapt`, because the planet with $M_{\rm p} = 100\,{\rm M}_\oplus$ did not undergo an intermittent migration jump.

4. Discussion

In this section we evaluate our results and their implications. We discuss the limitations of our method and possible ways to improve it.

4.1. Planet migration

We observe that regardless of the chosen EOS, the planet migrates in the vortex-assisted regime and may undergo one or several migration jumps. At its initial radial location, the planet has a mass of $M_{\rm p} \sim 2\,M_{\rm th}$ in models `iso`, `beta`, and `adapt` and $M_{\rm p} \sim 1.3\,M_{\rm th}$ in model `adapt-low-mass`. Since model `adapt` did not experience a migration jump, while models `beta` and `adapt-low-mass` did, we infer that the transition between the intermittent and type-II migration regimes depends on both planet mass and the local cooling timescale. This implies that modelling observed substructures in the context of migrating planets should be carried out carefully, including a prescription for cooling.
We also carried out models with β values of 0.01, 3, and 7.5, whose migration tracks are shown in Appendix A. The simulations with $\beta = 0.01$ and 3 also undergo intermittent migration when they reach the same radial location as `iso` and `beta`. This is most likely related to these models having comparable gap structures, due to the similar angular momentum flux profiles for $\beta = 1$ and 3 (Ziampras et al. 2026). The simulation with $\beta = 7.5$ does not experience any jumps and has a significantly different gap structure. This suggests that planets that open similar gap structures, regardless of the cooling timescale, undergo a jump at similar radii.
Nevertheless, we note that $\beta_{\rm fld}$ only cools locally. The full inclusion of FLD may be relevant, for example because $\beta_{\rm fld}$ overestimates the vortensity growth rate (Ziampras et al. 2024). This should be further investigated in future work.

4.2. Lifetime of radial structures

Most of the created dust structures remain visible in the intensity image at $t = 500$ kyr. Our isothermal simulation confirms the results of WB20, Mc19, and M26. As M26 point out in their analysis of different viscosity levels, long-lasting structures are only present for $\alpha \leq 10^{-4}$.
WB20 propose that the lifetime of these structures depends on the time spent in slow migration before or between jumps. To validate this statement in radiative discs, we additionally evaluated the simulations presented in Appendix A. Comparing the pressure maxima, minima, and surface density profiles, we find a clear correlation between the lifetimes of the structures and the duration of slow migration (vortex-assisted migration in this paper), in line with WB20. We find no direct correlation between the cooling timescale and the dissipation of pressure maxima (although we do identify an indirect connection, since the cooling timescale influences the planets' migration and number of jumps). This is expected because the lifetime of these structures is tied to the diffusion (i.e. viscous) timescale, which does not depend on the cooling timescale.

4.3. Vortex lifetimes

We observe large-scale vortices (~3–5 au in radial width) in models `iso` and `beta`, but not in models `adapt` or `adapt-low-mass`. They are decoupled from the planet, do not influence its migration, and persist for an average of 120 kyr in mode `iso` and 55 kyr in model `beta`. This is short compared to the disc's lifetime and the simulation runtime (consistent with Rometsch et al. 2021; Rafikov & Cimerman 2023). Thus, dust asymmetries caused by vortices are expected to be less commonly observed than ring-like structures. Additionally, they are only created in simulation with less realistic heating and cooling implementations.
An additional comparison of vortex lifetimes across the different simulation (including Appendix A) reveals that vortices survive only marginally longer for $\beta = 0.01$ than for $\beta = 1$, and no vortices are created if $\beta > 1$. This partially agrees with Rometsch et al. (2021), which finds the shortest vortex lifetimes for $\beta = 1$ and longer lifetimes for $\beta < 1$ than for $\beta > 1$. The planet mass used in both studies differs significantly, since Rometsch et al. (2021) used a Jupiter-mass planet. This may explain parts of the discrepancy.
We also observe that the locations of the large-scale vortices coincide with the created pressure maxima in models `iso` and `beta`. In model `adapt-low-mass`, the pressure maxima still appear but are considerably weaker, without any pre-existing large-scale vortices. Furthermore, the lifetime of the vortices does not determine the visibility and dissipation of the dust structures. Therefore, contrary to the results of M26, for discs with more realistic cooling timescales, pressure maxima are not strictly tied to large-scale vortices.

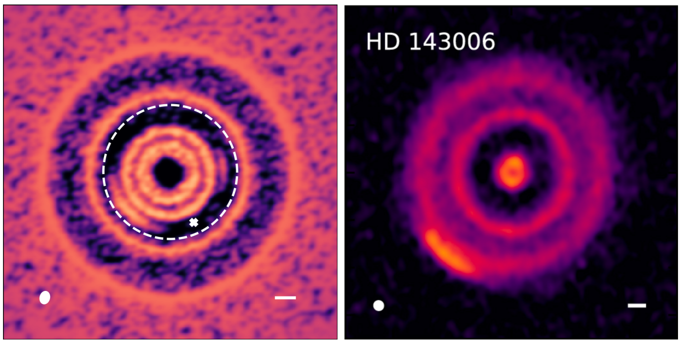

Fig. 15: Comparison of the convolved intensity image of model `iso` at t=300 kyr (left), placed at a distance of 100 pc, and HD 143006 (right). The image of HD 143006 is taken from Andrews et al. (2018). Both images include the 10 au scale bar.

4.4. Comparison to HD 143006

We find that the inner disc of model `iso` resembles the observations of HD 143006 (Andrews et al. 2018) reasonably well (Fig. 15). Both present an asymmetry, which in the case of model `iso` is created by material at the L5 Lagrange point, in addition to two rings in continuum emission. When omitting the outer disc of model `iso` and comparing the inner discs, they qualitatively resemble each other (i.e. our model uses a smaller beam, and the colour scale differs between the two panels). However, a locally isothermal model is far from realistic for modelling migration jumps in real discs (see the discussion in Sects. 3.2.2 onwards), and the ring expected to exist exterior to the planet's initial location (at $R \approx 60$ au) is missing. Hence, we caution against over-interpreting our results in the context of this system.

5. Conclusions

This paper demonstrates that one single migrating planet can produce several visible dust rings and gaps for different EOS. These structures remain visible for at least 300–400 kyr after their formation and likely persist for several hundred thousand years longer, a sizeable fraction of the median disc lifetime (Armitage 2020). Therefore, we can potentially explain the dynamical history of observed discs that show similar structures. We also confirm that the lifetimes of the produced dust structures depend on the time spent in slow migration before or between migration jumps (as in WB20), even in radiative discs.

We also see that cooling substantially affects the migration behaviour of a planet. The resulting asymmetric baroclinic forcing is an additional source of vortensity in the horseshoe region, which may accelerate migration if the planet has not yet opened a deep gap, as seen in models `beta` and `adapt`. The time required for a planet to clear its gap at its final location strongly depends on whether it has migrated far enough into the optically thick part of the disc, where cooling can assist in the gap-opening process (see Z25).

Some simulations showed large-scale vortices, always tied to the $\mathcal{IV}$ maxima. With an average vortex lifetime of only $\sim$ 90 kyr in our models, we should not expect protoplanetary discs with asymmetries caused by them to be as common as those without, if they are related to gap-opening planets. They also do not appear in the simulations with the most realistic cooling prescription, likely due to their faster dissipation due to cooling (e.g. Fung & Ono 2021; Rometsch et al. 2021). This does not include asymmetries created by other mechanisms, such as material left at the Lagrange point, which is observed in all simulations.

Our results indicate that migrating planets could be the origin of some of the substructure observed in millimetre emission with ALMA and highlight the importance of including a realistic cooling prescription when modelling this behaviour. As such, care should be taken when modelling and interpreting such structures. Differentiating between observable signatures of migrating or non-migrating planets, or of other origins, is beyond the scope of this paper but could be the focus of further work.

Acknowledgements. K.M.W. would like to thank Anna Penzlin for their advice and very insightful discussions. K.M.W, C.P.D and S.C.M. acknowledge support by the High Performance and Cloud Computing Group at the Zentrum für Datenverarbeitung of the University of Tübingen, the state of Baden-Württemberg through bwHPC and the German Research Foundation (DFG) through grant no INST 37/935-1 FUGG. K.M.W. and A.Z. acknowledge funding from the European Union under the European Union's Horizon Europe Research and Innovation Programme 101124282 (EARLYBIRD). Views and opinions expressed are, however, those of the authors only and do not necessarily reflect those of the European Union or the European Research Council. Neither the European Union nor the granting authority can be held responsible for them. All plots in this paper were made with the `python` package `matplotlib` Hunter 2007).

Data Availability

Data from our numerical models are available upon reasonable request to the corresponding author.

References

Andrews, S. M., Huang, J., Pérez, L. M., et al. 2018, ApJ, 869, L41, aDS Bibcode: 2018ApJ...869L..41A
Ansdell, M., Williams, J. P., Trapman, L., et al. 2018, ApJ, 859, 21
Armitage, P. J. 2020, Astrophysics of Planet Formation, 2nd edn. (Cambridge University Press)
Armitage, P. J. & Kley, W. 2019, SSAA, aDS Bibcode: 2019SAAS...45.....A
Armitage, P. J., Livio, M., & Pringle, J. E. 2001, MNRAS, 324, 705
Bae, J. & Zhu, Z. 2018a, ApJ, 859, 118
Bae, J. & Zhu, Z. 2018b, ApJ, 859, 119
Béthune, W., Lesur, G., & Ferreira, J. 2016, A&A, 589, A87
Crida, A., Baruteau, C., Gonzalez, J.-F., et al. 2025a, OJAp, 8, 115
Crida, A., Baruteau, C., Griveaud, P., et al. 2025b, OJAp, 8, 84
Crida, A., Morbidelli, A., & Masset, F. 2006, Icarus, 181, 587
Dominik, C., Min, M., & Tazaki, R. 2021, ASCL, ascl:2104.010, aDS Bibcode: 2021ascl.soft04010D
Dullemond, C. P., Birnstiel, T., Huang, J., et al. 2018, ApJ, 869, L46, aDS Bibcode: 2018ApJ...869L..46D
Dürmann, C. & Kley, W. 2015, A&A, 574, A52
Flock, M., Fromang, S., Turner, N. J., & Benisty, M. 2017, ApJ, 835, 230
Flock, M., Ruge, J. P., Dzyurkevich, N., et al. 2015, A&A, 574, A68, aDS Bibcode: 2015A&A...574A..68F
Fung, J. & Ono, T. 2021, ApJ, 922, 13
Goldreich, P. & Tremaine, S. 1979, ApJ, 233, 857, aDS Bibcode: 1979ApJ...233..857G
Goodman, J. & Rafikov, R. R. 2001, ApJ, 552, 793, aDS Bibcode: 2001ApJ...552..793G
Huang, J., Andrews, S. M., Dullemond, C. P., et al. 2018, ApJ, 869, L42, aDS Bibcode: 2018ApJ...869L..42H
Hubeny, I. 1990, ApJ, 351, 632, aDS Bibcode: 1990ApJ...351..632H
Hunter, J. D. 2007, CiSE, 9, 90
Jiang, H. & Ormel, C. W. 2023, MNRAS, 518, 3877
Kley, W. & Nelson, R. P. 2012, Annual Review of A&A, 50, 211, aDS Bibcode: 2012ARA&A..50..211K
Lega, E., Nelson, R. P., Morbidelli, A., et al. 2021, A&A, 646, A166
Long, F., Pinilla, P., Herczeg, G. J., et al. 2018, ApJ, 869, 17
Lovelace, R. V. E., Li, H., Colgate, S. A., & Nelson, A. F. 1999, ApJ, 513, 805, aDS Bibcode: 1999ApJ...513..805L
Masset, F. 2000, A&A Supplement Series, 141, 165, aDS Bibcode: 2000A&AS..141..165M
Masset, F. S. & Papaloizou, J. C. B. 2003, ApJ, 588, 494, aDS Bibcode: 2003ApJ...588..494M
Mathis, J. S., Rumpl, W., & Nordsieck, K. H. 1977a, ApJ, 217, 425
Mathis, J. S., Rumpl, W., & Nordsieck, K. H. 1977b, ApJ, 217, 425

McNally, C. P., Nelson, R. P., Paardekooper, S.-J., & Benítez-Llambay, P. 2019, MNRAS, 484, 728, aDS Bibcode: 2019MNRAS.484..728M
Meiners, S. C., Weiskopf, K. M., & Rometsch, T., e. a. 2026, A&A, submitted.
Menou, K. & Goodman, J. 2004, ApJ, 606, 520, aDS Bibcode: 2004ApJ...606..520M
Mignone, A., Bodo, G., Massaglia, S., et al. 2007, ApJs, 170, 228
Mignone, A., Zanni, C., Tzeferacos, P., et al. 2012, ApJs, 198, 7
Miranda, R. & Rafikov, R. R. 2020a, ApJ, 904, 121, aDS Bibcode: 2020ApJ...904..121M
Miranda, R. & Rafikov, R. R. 2020b, ApJ, 892, 65
Müller, T. W. A. & Kley, W. 2012, A&A, 539, A18, aDS Bibcode: 2012A&A...539A..18M
Nakagawa, Y., Sekiya, M., & Hayashi, C. 1986, Icarus, 67, 375
Öberg, K. I., Guzmán, V. V., Walsh, C., et al. 2021, ApJs, 257, 1
Ogilvie, G. I. & Lubow, S. H. 2002, MNRAS, 330, 950, aDS Bibcode: 2002MNRAS.330..950O
Orcajo, S., Cieza, L. A., Guilera, O., et al. 2025, ApJ, 984, L57, aDS Bibcode: 2025ApJ...984L..57O
Ostertag, D. & Flock, M. 2025, A&A, 695, L13
Owen, J. E. 2020, MNRAS, 495, 3160
Paardekooper, S. J. 2014, MNRAS, 444, 2031
Paardekooper, S.-J., Baruteau, C., & Kley, W. 2011, MNRAS, 410, 293
Paardekooper, S.-J., Lesur, G., & Papaloizou, J. C. B. 2010, ApJ, 725, 146, aDS Bibcode: 2010ApJ...725..146P
Pinilla, P., Benisty, M., & Birnstiel, T. 2012, A&A, 545, A81
Qian, Y. & Wu, Y. 2024, ApJ, 976, 5
Rafikov, R. R. 2002, ApJ, 572, 566, aDS Bibcode: 2002ApJ...572..566R
Rafikov, R. R. & Cimerman, N. P. 2023, MNRAS, 519, 5800
Riols, A., Lesur, G., & Menard, F. 2020, A&A, 639, A95
Roberts, M. J. O., Latter, H. N., & Lesur, G. 2025, MNRAS, 544, 1284
Rodenkirch, P. J., Rometsch, T., Dullemond, C. P., Weber, P., & Kley, W. 2021, A&A, 647, A174, aDS Bibcode: 2021A&A...647A.174R
Rometsch, T. 2023, coords2sigma
Rometsch, T., Jordan, L. M., Moldenhauer, T. W., et al. 2024, A&A, 684, A192, aDS Bibcode: 2024A&A...684A.192R
Rometsch, T., Rodenkirch, P. J., Kley, W., & Dullemond, C. P. 2020, A&A, 643, A87, aDS Bibcode: 2020A&A...643A..87R
Rometsch, T., Ziampras, A., Kley, W., & Béthune, W. 2021, A&A, 656, A130, aDS Bibcode: 2021A&A...656A.130R
Rosotti, G. P. 2023, New Astronomy Reviews, 96, 101674, aDS Bibcode: 2023NewAR..9601674R
Scardoni, C. E., Clarke, C. J., Rosotti, G. P., et al. 2022, MNRAS, 514, 5478, aDS Bibcode: 2022MNRAS.514.5478S
Shakura, N. I. & Sunyaev, R. A. 1973, A&A, 24, 337, aDS Bibcode: 1973A&A....24..337S
Smallwood, J. L., Lin, M.-K., Aly, H., Nealon, R., & Longarini, C. 2024a, MNRAS, 532, 1068
Smallwood, J. L., Nealon, R., Yen, H.-W., et al. 2024b, ApJl, 976, L23
Su, Z. & Bai, X.-N. 2024, ApJ, 975, 126
Sudarshan, P., Flock, M., Ziampras, A., Melon Fuksman, D., & Birnstiel, T. 2026, A&A, 706, A198
Teague, R., Benisty, M., Facchini, S., et al. 2025, ApJ, 984, L6, aDS Bibcode: 2025ApJ...984L...6T
Ueda, T., Flock, M., & Birnstiel, T. 2021, ApJl, 914, L38
Varnière, P. & Tagger, M. 2006, A&A, 446, L13, aDS Bibcode: 2006A&A...446L..13V
Villenave, M., Stapelfeldt, K. R., Duchêne, G., et al. 2022, ApJ, 930, 11, aDS Bibcode: 2022ApJ...930...11V
Wafflard-Fernandez, G. & Baruteau, C. 2020, MNRAS, 493, 5892, aDS Bibcode: 2020MNRAS.493.5892W
Wafflard-Fernandez, G. & Lesur, G. 2025, A&A, 696, A8
Weidenschilling, S. J. 1977, MNRAS, 180, 57
Youdin, A. N. & Goodman, J. 2005, ApJ, 620, 459
Zhang, K., Pérez, L. M., Pascucci, I., et al. 2025, ApJ, 989, 1, aDS Bibcode: 2025ApJ...989....1Z
Zhang, M., Huang, P., & Dong, R. 2024, ApJ, 961, 86, aDS Bibcode: 2024ApJ...961...86Z
Zhang, S. & Zhu, Z. 2020, MNRAS, 493, 2287, aDS Bibcode: 2020MNRAS.493.2287Z
Zhang, S., Zhu, Z., & Fairbairn, C. W. 2025, ApJl, 995, L33
Zhang, S., Zhu, Z., Huang, J., et al. 2018, ApJ, 869, L47, aDS Bibcode: 2018ApJ...869L..47Z
Ziampras, A., Cordwell, A. J., Rafikov, R. R., & Nelson, R. P. 2026, A&A, 705, A194
Ziampras, A., Dullemond, C. P., Birnstiel, T., Benisty, M., & Nelson, R. P. 2025a, MNRAS, 540, 1185, aDS Bibcode: 2025MNRAS.540.1185Z
Ziampras, A., Kley, W., & Dullemond, C. P. 2020, A&A, 637, A50, aDS Bibcode: 2020A&A...637A..50Z
Ziampras, A., Nelson, R. P., & Paardekooper, S.-J. 2024, MNRAS, 528, 6130, aDS Bibcode: 2024MNRAS.528.6130Z
Ziampras, A., Nelson, R. P., & Paardekooper, S.-J. 2025b, MNRAS, 542, 1685, aDS Bibcode: 2025MNRAS.542.1685Z
Ziampras, A., Nelson, R. P., & Rafikov, R. R. 2023, MNRAS, 524, 3930, aDS Bibcode: 2023MNRAS.524.3930Z

Appendix A: Migration tracks of different β-cooling simulations

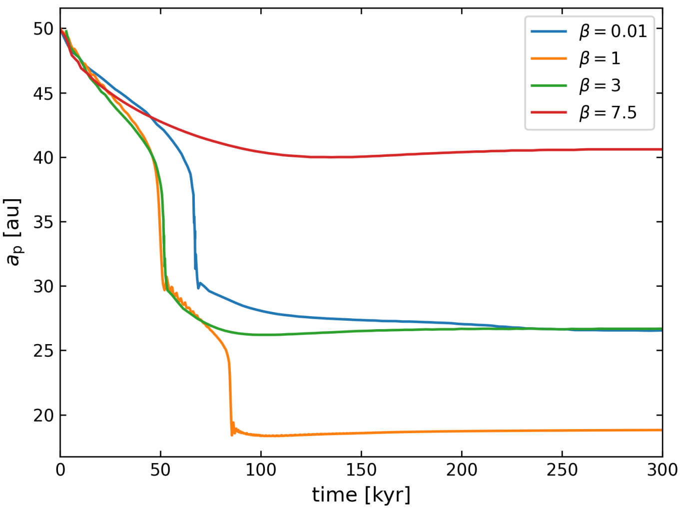

Fig. A.1: Semi-major axis evolution of model `beta` compared to simulations with $\beta = 0.01$, 3 and 7.5.

Figure A.1 displays the semi-major axis evolution of simulations with different constant β-cooling timescales, compared to model `beta`. We ran these additional models to further analyse the radius, where the planet undergoes its first migration jump as well as the vortex and dust structure lifetimes as a function of the cooling timescale for our analysis in Sects. 4.1 and 4.3. We observe that the planet in the simulations with $\beta = 0.01$ and 3 undergoes one migration jump at the same radius as model `beta`. Unsurprisingly, the simulation with $\beta = 0.01$ is very similar to our isothermal model. On the other hand, the planet in the simulation with $\beta = 7.5$ does not undergo a migration jump, since the vortices did not accelerate the planet's migration sufficiently for it to catch up with its own gap.

Appendix B: Baroclinic forcing and low-vortensity ribbons

In Sect. 3.2.2 we discussed the mechanism behind the formation of a high-$\mathcal{IV}$ (i.e. low-vortensity) ribbon exterior to the planet's orbit, notably outside of the planet's horseshoe region. As mentioned in the main text, this ribbon is the product of significant baroclinic forcing as gas interacts with the shock front at $\phi \approx \phi_\mathrm{p}$ before shearing past the planet. This suggests that there should be a clear dependence of this forcing term on the temperature gradient across the shock $\partial T/\partial\phi$, and, therefore, on the cooling timescale.

To investigate this, we ran a set of five models using the `PLUTO` code (Mignone et al. 2007, 2012), mirroring the setup in Sect. 3.2.2 but using a lower resolution of $N_R \times N_\phi = 256 \times 768$ and holding the planet fixed at 50 au for 10 orbits. Each of these five models uses a different cooling prescription: locally isothermal ($\beta = 0$), cooling with $\beta \in [0.1, 1, 10]$, and adiabatic ($\beta \to \infty$). We then compute the individual components of the baroclinic forcing term at $t = 10$ planetary orbits as in Eq. (9):

$$\mathcal{S}_1 = \frac{P}{TR\Sigma^3}\frac{\partial\Sigma}{\partial R}\frac{\partial T}{\partial\phi}, \quad \mathcal{S}_2 = -\frac{P}{TR\Sigma^3}\frac{\partial\Sigma}{\partial\phi}\frac{\partial T}{\partial R}, \tag{B.1}$$

with $\mathcal{S} = \mathcal{S}_1 + \mathcal{S}_2$. The results are shown in Fig. B.1, which illustrates that this baroclinic forcing does indeed depend strongly on the prescribed cooling timescale. In particular, we find that the forcing responsible for the high-$\mathcal{IV}$ ribbons (identified by green patches close to the planet in the bottom row, as in Fig. 9) peaks for $\beta \sim 1$ (at least among the values tested), in line with the discussion in Sect. 3.2.2.

By plotting the individual components of $\mathcal{S}$, we can identify that this ribbon is indeed driven by term $\mathcal{S}_1$ (top row) and is mostly sensitive to $\partial T/\partial\phi$ (see also Fig. 7). Since $\partial T/\partial\phi = 0$ in our locally isothermal models, this term is completely absent there, hence the lack of a high-$\mathcal{IV}$ ribbon in the model discussed in Sect. 3.2.1. We can further note that the term $\mathcal{S}_2$ (middle row) peaks within the horseshoe region (here marked approximately by black dashed curves), not contributing to this behaviour. Instead, these peaks are related to the mechanism described in Ziampras et al. (2024), driving vortensity growth within the horseshoe region and contributing to a negative dynamical corotation torque in addition to the vortex-assisted refilling of the gap described in the main text. Ultimately, both processes operate in tandem to accelerate migration inwards, explaining the more vigorous "jumping" that the planet experiences in model `beta`.

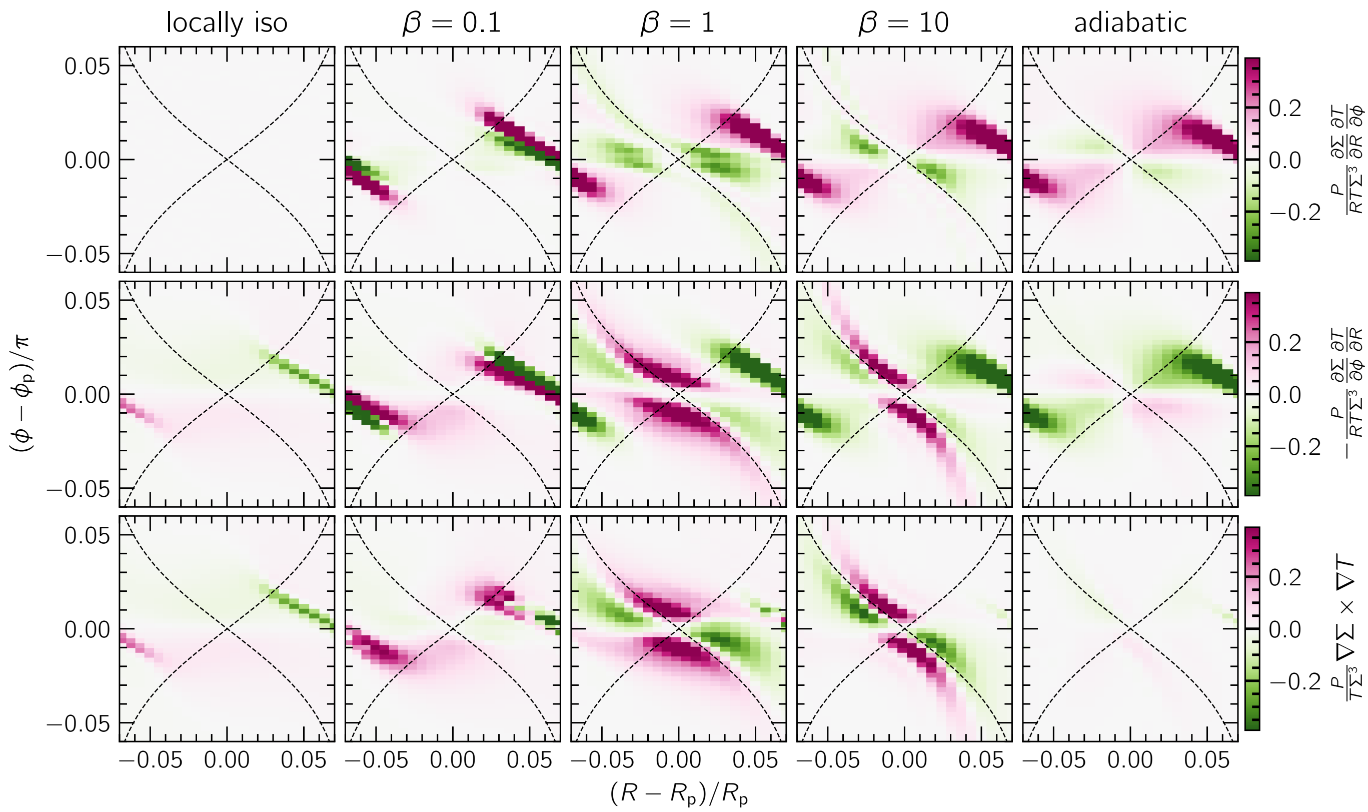

Fig. B.1: Different components of the baroclinic forcing term as in Eqs. (9) & (B.1) for our PLUTO models with different cooling prescriptions. Dashed curves follow the edges of the horseshoe region, with the planet at the centre of each panel. We can identify the vortensity sourcing within the horseshoe region as in Ziampras et al. (2024) (purple patches at $R \approx R_p$) as well as the vortensity sinks associated with the high-$\mathcal{IV}$ ribbons in Fig. 6 for $\beta \sim 1$ (green patches at $\phi \approx \phi_p$).